Quantification of anisotropy and orientation in 3D electron microscopy and diffusion tensor imaging in injured rat brain

Salo, Raimo A.

2018-05-15

Salo , R A , Belevich , I , Manninen , E , Jokitalo , E , Gröhn , O & Sierra , A 2018 , ' Quantification of anisotropy and orientation in 3D electron microscopy and diffusion tensor imaging in injured rat brain ' , NeuroImage , vol. 172 , pp. 404-414 . https://doi.org/10.1016/j.neuroimage.2018.01.087

http://hdl.handle.net/10138/239258
https://doi.org/10.1016/j.neuroimage.2018.01.087

Accepted Manuscript

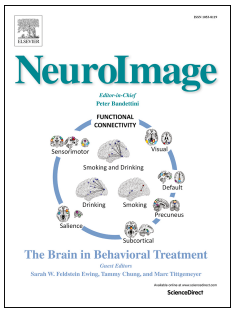

Quantification of anisotropy and orientation in 3D electron microscopy and diffusion tensor imaging in injured rat brain

Raimo A. Salo, Ilya Belevich, Eppu Manninen, Eija Jokitalo, Olli Gröhn, Alejandra Sierra

PII: S1053-8119(18)30087-9

DOI: 10.1016/j.neuroimage.2018.01.087

Reference: YNIMG 14700

To appear in: *NeuroImage*

Received Date: 5 September 2017

Revised Date: 16 January 2018

Accepted Date: 30 January 2018

Please cite this article as: Salo, R.A., Belevich, I., Manninen, E., Jokitalo, E., Gröhn, O., Sierra, A., Quantification of anisotropy and orientation in 3D electron microscopy and diffusion tensor imaging in injured rat brain, *NeuroImage* (2018), doi: 10.1016/j.neuroimage.2018.01.087.

Quantification of anisotropy and orientation in 3D electron microscopy and diffusion tensor imaging in injured rat brain

Raimo A. Salo[1], Ilya Belevich[2], Eppu Manninen[1], Eija Jokitalo[2], Olli Gröhn[1], and Alejandra Sierra[1]

[1]*Biomedical Imaging Unit, A. I. Virtanen Institute for Molecular Sciences, University of Eastern Finland, PO Box 1627, FI-70211 Kuopio, Finland*

[2]*Electron Microscopy Unit, Institute of Biotechnology, University of Helsinki, PO Box 56, FI-00014 Helsinki, Finland*

Corresponding author: Dr. Alejandra Sierra

A. I. Virtanen Institute for Molecular Sciences, University of Eastern Finland

PO Box 1627, FI-70211 Kuopio, Finland

Tel: +358-40-355 2219

Fax: +358-17-16 3030

e-mail: alejandra.sierralopez@uef.fi

Abbreviations: 3D-FT, three dimensional Fourier transform-based analysis; AI, anisotropy index; DEC, directionally encoded coloured map; DTI, diffusion tensor imaging; EM, electron microscopy; FA, fractional anisotropy; HM, high magnification; LM; low magnification; MRI, magnetic resonance imaging; SBEM, serial block-face scanning electron microscopy; TBI, traumatic brain injury; V1, principal eigenvector; VOI, volume-of-interest.

Abstract

Diffusion tensor imaging (DTI) reveals microstructural features of grey and white matter non-invasively. The contrast produced by DTI, however, is not fully understood and requires further validation. We used serial block-face scanning electron microscopy (SBEM) to acquire tissue metrics, i.e., anisotropy and orientation, using three-dimensional Fourier transform-based (3D-FT) analysis, to correlate with fractional anisotropy and orientation in DTI. SBEM produces high-resolution 3D data at the mesoscopic scale with good contrast of cellular membranes. We analysed selected samples from cingulum, corpus callosum, and perilesional cortex of sham-operated and traumatic brain injury (TBI) rats. Principal orientations produced by DTI and 3D-FT in all samples were in good agreement. Anisotropy values showed similar patterns of change in corresponding DTI and 3D-FT parameters in sham-operated and TBI rats. While DTI and 3D-FT anisotropy values were similar in grey matter, 3D-FT anisotropy values were consistently lower than fractional anisotropy values from DTI in white matter. We also evaluated the effect of resolution in 3D-FT analysis. Despite small angular differences in grey matter samples, lower resolution datasets provided reliable results, allowing for analysis of larger fields of view. Overall, 3D SBEM allows for more sophisticated validation studies of diffusion imaging contrast from a tissue microstructural perspective.

Introduction

Despite the wide use of diffusion tensor imaging (DTI) in clinics and research, the biological interpretation of the contrast produced by DTI is lacking. Among all of the magnetic resonance imaging (MRI) techniques, DTI is the method of choice for non-invasively obtaining microstructural information from brain tissue. DTI probes the tissue microstructure by measuring the diffusion of water, i.e., the random motion of water molecules, restricted by tissue microstructures (**Basser et al., 1994; Basser and Pierpaoli, 1996; Le Bihan, 2003**). A typical voxel in DTI, e.g., 100 x 100 x 100 μm^3 in rodent brain or 2 x 2 x 2 mm^3 in humans, is highly heterogeneous, however, and contains a variety of cellular structures whose contribution to the restricted diffusion of the water molecules is only partially understood.

Histological characterization, mainly using light microscopy, has predominantly been used to interpret the DTI quantitative parameters in terms of the underlying cellular structures in normal and pathological brain (**Dauguet et al. 2007; Leergaard et al., 2010; Wang et al., 2014, Aggarwal et al., 2015; Sierra et al., 2015**). Although the combination of DTI and conventional histology provides insights into the DTI contrast, light microscopy has several major restrictions in terms of interpreting the imaging contrast, such as inability to produce three-dimensional (3D) images, staining specificity, and spatial resolution. Recent advances have made 3D microscopic data available for correlation studies, such as confocal light microscopy (**Jespersen et al. 2012; Khan et al., 2015; Schilling et al., 2016**), polarised light microscopy (**Axer et al., 2011; Axer et al., 2016**), serial optical coherence scanning (**Wang et al., 2014; Wang et al., 2015**), or whole-brain multiphoton imaging in combination with clearing tissue techniques (**Chang et al., 2016; Chang et al., 2017**). The main physical barriers for water molecule motion are the cellular membranes. The resolution of light microscopy in the techniques mentioned above, however, cannot reliably

resolve individual membranes. Even with the use of lipophilic carbocyanine dyes (e.g., DiI), which label cellular membranes (**Chazotte, 2011**), only "macrostructural information" of the cellular barriers for water molecules can be determined (**Budde et al., 2011; Khan et al., 2015**). Another limitation of the histochemistry and immunohistochemistry staining methods used for light microscopy is that the dyes and antibodies can be used to trace only a limited number of cellular components within the same preparation.

Electron microscopy (EM) provides the contrast and high resolution required for visualising cellular membranes, but has not reached a large enough spatial scale to cover the scale of the MRI voxel. Serial block-face scanning electron microscopy (SBEM) produces 3D datasets in high-resolution at the mesoscopic scale (on the order of a few hundred micrometres) (**Denk and Horstmann, 2004**). Imaging of the block-face in SBEM is performed by scanning electron microscopy (SEM) using back-scattered electron detection and low beam energies (**Denk and Horstmann, 2004; Helmstaedter et al. 2008**). An ultra-microtome inside a vacuum chamber repeatedly removes the top section of a block-face using a diamond knife. In each round, the newly exposed block-face is imaged. As the enhanced tissue staining protocol for EM allows for visualisation of all the membranes, SBEM is an ideal method for obtaining insight into the 3D tissue microstructural environment with a large field of view that is comparable to the voxel size of MRI.

Fourier transform-based (FT) analysis extracts information about the organization and orientation of structures of an image (**Josso et al., 2005; Marquez, 2006**). In a photomicrograph, FT analysis uses the intensity patterns of the stained cellular structures to measure their anisotropy and orientation. As the FT method is intrinsically different from DTI, anisotropy values from FT analysis might differ from DTI fractional anisotropy (FA) values, but these two measures

are expected to correlate. Previous FT analysis work studied microstructural changes in histological photomicrographs of normal and pathological brain tissue (**Budde et al., 2011; Salo et al., 2017**). These studies demonstrated that FT analysis offers a direct and quantitative assessment of the anisotropy and orientation of the microstructures within a tissue, allowing investigators to obtain insight into the source of the DTI contrast.

In this study, we exploited the potential of SBEM to provide 3D high-resolution images of diffusion-restricting structures in tissue. To obtain quantitative metrics comparable to DTI data, we extended the existing 2D Fourier analysis to 3D Fourier transform-based analysis (3D-FT). We calculated the anisotropy and orientation in the SBEM volumes of the cingulum, corpus callosum, and perilesional cortex in a sham-operated rat and rats with severe traumatic brain injury (TBI). Finally, we compared the anisotropy and orientation data obtained from SBEM to the fractional anisotropy (FA) and orientation data obtained from DTI of the same samples. This method may provide novel insights into the microstructural environment probed by water molecules in diffusion MRI.

Materials and methods

Animals. Three adult male Sprague-Dawley rats (10-weeks old, weight 300-350 g, Harlan Netherlands B.V., Horst, Netherlands) were used in the study. The animals were housed in a room (22 ± 1°C, 50%-60% humidity) with 12 h light/dark cycle and free access to food and water. All animal procedures were approved by the Animal Care and Use Committee of the Provincial Government of Southern Finland and performed according to the guidelines set by the European Community Council Directives 86/609/EEC.

Traumatic brain injury model. TBI was induced by lateral fluid percussion injury (**Kharatishvili et al., 2006**). Rats were anesthetised with a single intraperitoneal injection (6 ml/kg) of a mixture of

sodium pentobarbital (58 mg/kg), magnesium sulphate (127.2 mg/kg), propylene glycol (42.8%), and absolute ethanol (11.6%). A craniotomy (∅ 5 mm) was performed between bregma and lambda on the left convexity (anterior edge 2.0 mm posterior to bregma; lateral edge adjacent to the left lateral ridge). Lateral fluid percussion injury was induced by a transient fluid pulse impact (21-23 ms) against the exposed intact dura using a fluid-percussion device. The impact pressure was adjusted to 3.2-3.4 atm to induce a severe injury. Sham-operation included all the surgical procedures except the impact.

Tissue processing. EM studies are challenging because of the labour-intensive sample preparation, which limits the number of samples that can be analysed. For this proof-of-concept study, we prepared a total of 12 samples, from ipsi- and contralateral cingulum/corpus callosum and perilesional cortex of one sham-operated and two TBI rats (TBI #1 and TBI #2). The three rat brains and the samples were prepared according to a carefully planned protocol including both DTI and SBEM to preserve the ultrastructure of the tissue.

Five months after TBI or sham operation, the rats were transcardially perfused using 0.9% NaCl (30 ml/min) for 2 min followed by 4% paraformaldehyde (PFA; 30 ml/min) at 4°C for 25 min. The brains were removed from the skull and post-fixed in 4% PFA/1% glutaraldehyde overnight at 4°C. The brains were placed in 0.9% NaCl for at least 12 h to remove excess PFA.

***Ex vivo* DTI and data processing.** The rat brains were scanned *ex vivo* in a vertical 9.4 T/89 mm magnet (Oxford Instruments PLC, Abingdon, UK) interfaced with a DirectDrive console (Varian Inc., Palo Alto, CA, USA) using a quadrature volume RF-coil (Ø = 20 mm; Rapid Biomedical GmbH, Rimpar, Germany) as both transmitter and receiver. During imaging, the brains were immersed in perfluoropolyether (Solexis Galden®, Solvay, Houston, TX, USA) to avoid signals from the surrounding area.

The data were acquired using a 3D segmented spin-echo EPI sequence (TR = 1000 ms, TE = 35 ms, data matrix 128 x 96 x 96, FOV 19.2 x 14.4 x 14.4 mm^3, resolution 0.150 x 0.150 x 0.150 mm^3) with four segments. The acquisition comprised a total of 129 volumes, with 3 sets of 42 uniformly distributed directions with diffusion weighting (b-values = 2000, 3000, and 4000 s/mm^2, δ = 6 ms, Δ = 11.5 ms) and three images without diffusion weighting. The total scan time was 14 h, 24 min, and 27 s. The samples were imaged at room temperature, and the temperature variation of the sample over the DTI measurement period as measured in separate experiments under identical conditions was less than ±0.25°C (**Laitinen et al., 2010**).

The DTI data were first converted to NIfTI format, and pre-processing and analyses were performed using the FMRIB Software Library (FSL 5.0, http://fsl.fmrib.ox.ac.uk/fsl/fslwiki). Pre-processing steps consisted of brain extraction using the FSL Brain Extraction Tool, followed by simultaneous motion correction and eddy current correction using the FSL eddy tool. The analysis was performed in a single DTIFIT run with all the different b-values specified simultaneously using ordinary least-squares fitting. The maps acquired were FA, the principal eigenvector (V1), the second eigenvector (V2), the third eigenvector (V3), the first eigenvalue (L1), the second eigenvalue (L2), the third eigenvalue (L3), and directionally-encoded fractional anisotropy map (DEC-FA) (**Figure 1A**).

Tissue preparation for SBEM. After the *ex vivo* DTI, the brains were placed in 0.9% NaCl for at least 4 h to remove excess perfluoropolyether, and were then sectioned into 1-mm thick coronal sections with a vibrating blade microtome (VT1000s, Leica Instruments, Germany). Sections from -3.80 mm from bregma from each brain were selected and further dissected into smaller samples containing the areas of interest. We collected four samples from each brain: ipsilateral and contralateral perilesional cortex, and ipsilateral and contralateral cingulum/corpus callosum

(**Figure 1B**). Note that the dissected areas were bigger than that required for imaging to ensure proper co-registration, avoid tissue damage and deformation, and facilitate the selection of the area to be imaged in SBEM (**Figure 1D**). Photomicrographs of both 1-mm thick sections and dissected samples to use in co-registration were obtained using a stereo microscope equipped with a Nikon DXM1200F digital camera. The total time for sectioning and photomicrography was approximately 1 h.

The dissected samples were stained using an enhanced staining protocol (**Deerinck et al., 2010**). First, the samples were immersed in 2% PFA in 0.15 M cacodylate buffer containing 2 mM calcium chloride (pH = 7.4), and then washed 5 times for 3 min in cold 0.15 M cacodylate buffer containing 2 mM calcium chloride (pH = 7.4). After washing, the samples were incubated for 1 h on ice in a solution containing 3% potassium ferrocyanide in 0.3 M cacodylate buffer with 4 mM calcium chloride combined with an equal volume of 4% aqueous osmium tetroxide. Next, they were washed in ddH_2O at room temperature (5 x 3 min). Thereafter, the samples were placed in a solution of 0.01 mg/ml thiocarbohydrazide solution at room temperature for 20 min. Samples were then rinsed again in ddH_2O (5 x 3 min), and placed in 2% osmium tetroxide in ddH_2O at room temperature. Following the second exposure to osmium, the samples were washed in ddH_2O (5 x 3 min), and then incubated in 1% uranyl acetate overnight at 4°C. The following day, after the samples were washed in ddH_2O (5 x 3 min) and *en bloc* Walton´s lead aspartate staining was performed. In this step, the samples were incubated in 0.0066 mg/ml lead nitrate in 0.03 M aspartic acid (pH = 5.5) at 60°C for 30 min, after which the samples were washed in ddH_2O at room temperature (5 x 3 min), and dehydrated using ice-cold solutions of freshly prepared 20%, 50%, 70%, 90%, 100%, and 100% (anhydrous) ethanol for 5 min each, and finally placed in ice-cold anhydrous acetone at room temperature for 10 min. Embedding was performed in Durcupan ACM resin (Electron Microscopy Sciences, Hatfield, PA, USA). First, the samples were placed into 25%

Durcupan#1 (without component C):acetone, then into 50% Durcupan#1:acetone, and after into 75% Durcupan#1:acetone overnight. On the following day, they were placed in 100% Durcupan#1 for 2 h in a 50°C oven (2 times), and into 100% Durcupan#2 (4-component mixture) for 2 h in a 50°C oven. Finally, the samples were embedded in 100% Durcupan#2 into Beem embedding capsules (Electron Microscopy Sciences) and baked in a 60°C oven for 48 h.

Prior to mounting the specimens, the excess resin in the hardened tissue blocks was trimmed. Then, 5 semi-thin 500-nm sections were sectioned from the face of the block. The first section was stained with toluidine blue, and the remaining 4 sections were stored for future histological characterization. The fifth section was use for co-registration and selection of the area of interest for imaging (**Figure 1D**). After selecting the area, the blocks were further trimmed in a pyramidal shape with base of 1 x 1 mm^2 and top (face) of approximately 600 x 600 μm^2, which assured the stability of the block during the cutting in the SBEM microscope. The tissue was exposed on all four sides, bottom, and top of the pyramid. The blocks were then mounted on aluminium specimen pins using conductive silver epoxy (CircuitWorks CW2400). Silver paint (Ted Pella, Redding, CA, USA) was used to electrically ground the exposed block edges to the aluminium pin, except for the block face or the edges of the embedded tissue. Then, the entire surface of the specimen was sputtered with a thin layer of platinum coating to improve conductivity and reduce charging during the sectioning process.

SBEM data acquisition. All SBEM data were acquired on an SEM microscope (Quanta 250 Field Emission Gun; FEI Co., Hillsboro, OR, USA), equipped with 3View system (Gatan Inc., Pleasanton, CA, USA) using a backscattered electron detector (Gatan Inc., Pleasanton, CA, USA). The top of the mounted block or face was the x-y plane, and the z-direction was the direction of the cutting.

When the mounted block was positioned in the microscope, we took an overview image of the volume-of-interest (VOI) to be scanned (**Figure 1F**).

All the samples were imaged with a beam voltage of 2.5 kV and a pressure of 0.15 Torr. In each sample, we obtained two datasets that were collected simultaneously (**Figure 1G**). One dataset, called low magnification (LM), was imaged at a magnification between 450x to 550x and acquired with a resolution of 50.0 x 50.0 x 50.0 nm^3 amounting to an area of 102.4 x 204.8 μm^2 in the x-y plane and a mean distance of 65.4 ± 2.1 µm in the z-direction. The second dataset, called high magnification (HM), was imaged with higher magnification between 6500x to 7200x and acquired with higher resolution of 13.8-16.8 x 13.8-16.8 x 50 nm^3 amounting to an area of 14.0-17.2 x 14.0-17.2 μm^2 in the x-y plane and an average distance of 30.2 ± 3.7 µm in the z-direction. After imaging, Microscopy Image Browser (MIB; http://mib.helsinki.fi; **Belevich et al., 2016**) was used to process and align the SBEM image stacks. An example visualization, a 3D low magnification dataset from contralateral perilesional cortex of the sham-operated rat, is shown in **Supplementary video 1**.

Co-registration of DTI and SBEM data. The DTI and SBEM datasets were co-registered to re-position the SBEM datasets into the brain reference frame and to select DTI voxels that spatially corresponded with the SBEM datasets. For the co-registration, we used affine transformations involving translation, rotation, and non-uniform voxel stretching to account for tissue shrinkage. First, we manually co-registered the DEC-FA images (**Figure 1A**) into photomicrographs of 1-mm thick sections of the whole brain (**Figure 1B**) using Amira software (version 5.6.0; FEI Co.). This co-registration provides an estimate of the 3D rotations between the DTI data and whole brain sections (**Figure 1C**). The second step was to co-register the SBEM datasets to the 1-mm thick sections. The fifth semi-thin section (**Figure 1D**) was first co-registered to the dissected tissue

sample using landmarks, such as tissue borders. Then, the SBEM overview (**Figure 1F**) was co-registered to the fifth semi-thin section using local landmarks, such as vessels and cell bodies. The SBEM low and high magnification datasets (**Figure 1G**) were finally co-registered to the SBEM overview. Combining these steps provides the rotation of SBEM datasets into the rotational frame of reference of the 1-mm thick sections.

3D Fourier analysis. The 3D-FT analysis presented here is an extension and modification of an existing 2D Fourier analysis (**Josso et al. 2005; Marquez 2006; Budde et al., 2011**). The datasets were first subdivided into smaller volumes of 255 x 255 x 255 voxels to avoid excessive memory use. Each 3D stack of the sub-volume images (**Supplementary video 2A**) was first filtered with a 3D ball-like Tukey window:

$$\omega_0 = \begin{cases} 1 & r < \dfrac{(1-\alpha)N+1}{2} \\ 0.5\left[1+\cos\left(\pi\left(\dfrac{2r-1}{\alpha N}-\dfrac{1}{\alpha}+1\right)\right)\right] & \dfrac{(1-\alpha)N+1}{2} \le r < \dfrac{N+1}{2}, \\ 0 & \dfrac{N+1}{2} \le r \end{cases} \text{, where}$$

where $0 \le \alpha \le 1$ (we set $\alpha = 0.2$), and

$$r = \sqrt{\left(x-\frac{N-1}{2}\right)^2+\left(y-\frac{N-1}{2}\right)^2+\left(z-\frac{N-1}{2}\right)^2},$$

where *x*, *y*, and *z* define the voxel location in Cartesian coordinates. This was performed to avoid edge effects in the Fourier space (**Supplementary video 2B**). Second, a fast version of a discrete 3D Fourier transform was computed,

$$F(u,v,w) = \sum_{x=0}^{M-1}\sum_{y=0}^{N-1}\sum_{z=0}^{P-1} f(x,y,z)e^{-i2\pi\left(\frac{ux}{M}+\frac{vy}{N}+\frac{wz}{P}\right)},$$

where *u*, *v*, and *w* are the spatial frequencies and where *M*, *N*, and *P* are the number of samples in each direction (**Supplementary video 2C**). Third, we computed the power spectrum, $P_{sub}(u,v,w) = |F(u,v,w)|^2$.

All of the power spectra from the sub-volumes were then summed and an amplitude spectrum created: $A(u,v,w) = \sqrt{\sum P_{sub}(u,v,w)}$. A $3 \times n$ scatter matrix X, describing the orientation distribution of A, was then formed using a Cartesian to spherical coordinate transform as a base and replacing voxel distance with values from A:

$$X = \begin{pmatrix} A(\theta_1,\varphi_1,\rho_1)\sin\theta_1\cos\varphi_1 & \cdots & A(\theta_n,\varphi_n,\rho_n)\sin\theta_n\cos\varphi_n \\ A(\theta_1,\varphi_1,\rho_1)\sin\theta_1\sin\varphi_1 & \cdots & A(\theta_n,\varphi_n,\rho_n)\sin\theta_n\sin\varphi_n \\ A(\theta_1,\varphi_1,\rho_1)\cos\theta_1 & \cdots & A(\theta_n,\varphi_n,\rho_n)\cos\theta_n \end{pmatrix},$$

where $\rho_i = \sqrt{x_i^2 + y_i^2 + z_i^2}$, $\theta_i = \tan^{-1}\left(\frac{\sqrt{x_i^2+y_i^2}}{z_i}\right)$, $\varphi_i = \tan^{-1}\left(\frac{y_i}{x_i}\right)$. Furthermore, the range of amplitudes included in *X* was restricted by requiring that $15sz < \rho_i < 140sz$, where *sz* is the in-plane voxel length. A covariance matrix was then formed as $C = XX^T$. Eigen decomposition, $C = QDQ^{-1}$, gave the eigenvalues, $\mathrm{diag}(D) = (\lambda_1, \lambda_2, \lambda_3)$, and eigenvectors, column vectors of *Q*, of the covariance matrix. The eigenvectors and values form an ellipsoid model of the Fourier space (**Supplementary video 2D**). The anisotropy index (AI) was computed from the eigenvalues by:

$$AI = \sqrt{\frac{1}{2}}\frac{\sqrt{(\lambda_1-\lambda_2)^2 + (\lambda_2-\lambda_3)^2 + (\lambda_3-\lambda_1)^2}}{\sqrt{\lambda_1^2+\lambda_2^2+\lambda_3^2}}.$$

The orientation information was given by the eigenvectors. As FT places higher amplitudes and frequencies in the directions where there were more obstacles (**Supplementary video 2D**), the order of the eigenvectors needed to be reversed to correspond to diffusion orientation eigenvectors in the DTI (**Supplementary video 2E**).

The 3D-FT analysis was implemented in-house using Matlab (Matlab R2015b, Mathworks Inc., Natick, MA, USA). The 3D visualisation was produced using Amira software (version 5.6.0; FEI Co.).

Selection of volume-of-interest in SBEM datasets. The white matter SBEM datasets contained approximately two-thirds of the corpus callosum and one-third of the cingulum. We selected two VOIs in each dataset, one in the cingulum and another in the corpus callosum (**Figure 2A**). The cingulum VOI size was between 51.6-60.0 x 94.0-102.4 μm^2 in the x-y plane and between 51.0-69.2 μm in the z-direction. In the corpus callosum, the VOI size was 120.0 x 94.0-102.4 μm^2 in the x-y plane and between 51.0-69.2 μm in the z-direction. The VOI from the contralateral corpus callosum of TBI #1 was smaller than the other VOIs from this area (78.2 x 94.2 x 54.3 μm^3).

The SBEM datasets from the perilesional cortex contained mainly cortical layer VI and a fraction of the external capsule. We selected a VOI comprising the whole volume of layer VI in the dataset, excluding the external capsule (**Figure 3A**). The perilesional cortex VOI size was 150.0 x 96.0-102.4 μm^2 in the x-y plane and 62.0-75.9 μm in the z-direction. The VOIs from both the ipsilateral and contralateral cortex of TBI #1 were smaller than those in the other samples (69.0 x 94.2 x 75.9 μm^3 and 69.0 x. 94.2 x 70 μm^3, respectively).

When comparing high and low magnification 3D-FT to each other, the entire high magnification datasets were used, whereas the low magnification datasets were cropped to contain the same volume as the high magnification datasets.

Tissue metrics extracted from SBEM datasets. From 3D-FT of the SBEM datasets, we obtained AI, which was compared to FA obtained from the corresponding voxel in DTI. For the orientation, we performed a comparison between DTI and SBEM orientation of the vectors. Angular difference was defined as the difference in angle between DTI orientation vectors and corresponding Fourier

analysis orientation vectors. For visualization of the results, we computed the diffusion ellipsoids using eigenvector and eigenvalue information from the DTI and SBEM datasets.

Results

Qualitative and quantitative analyses of white matter: cingulum and corpus callosum

Cingulum. Figure 2 shows representative SBEM images of the ipsilateral cingulum and corpus callosum from the sham-operated and TBI #2 animals. Qualitative observations of the datasets revealed that the cingulum generally showed a decrease in axonal diameter and thinning of myelin sheaths after TBI (**Figure 2B**) compared with the sham-operated rat (**Figure 2A**). We also observed an increase in the number of cell bodies present in the cingulum volume, which might be indicative of gliosis (**Figure 2B**). These observations were consistent for both TBI rats.

The location of the SBEM sample in the DEC-FA map is shown in **Figure 4**. After the injury (**Figure 4D**), FA values decreased while the orientation of the water diffusion remained rostro-caudal as compared to the corresponding voxel in the sham-operated animal (**Figure 4A**). Diffusion ellipsoids, anisotropy values, and angular differences between DTI and SBEM orientation vectors from the ipsi- and contralateral cingulum in sham-operated and TBI rats are shown in **Figure 5**. The ipsilateral FA (TBI #1 = 0.68; TBI #2 = 0.51) decreased after TBI compared to the contralateral side in the same rats (TBI #1 = 0.72; TBI #2 = 0.71), or to the ipsilateral (0.77) and contralateral (0.73) sides of the sham-operated rat (**Figure 5A**). In the TBI animals, AI values presented a similar pattern to the FA values. Ipsilateral AI values (TBI #1 = 0.37; TBI #2 = 0.40) decreased in the cingulum of TBI rats as compared to contralateral cingulum in the same rats (TBI #1 = 0.47; TBI #2 = 0.50), or to the ipsi- and contralateral cingulum of the sham-operated rat (Ipsi = 0.49; Contra = 0.51; **Figure 5A**).

The angular difference between the orientation of the principal eigenvectors from DTI and SBEM varied between 5.6° and 16.7° (**Figure 5A**). Despite the angular difference, the diffusion ellipsoids showed that the main orientation obtained from these two methods were consistent. In both DTI and SBEM the orientations of the principal eigenvector were rostro-caudal in both hemispheres in the sham-operated rat. While the orientation remained rostro-caudal in the TBI animals, there was a small contribution of the dorso-ventral orientation, which was more evident ipsilaterally in TBI #2 (**Figure 5A**).

Corpus callosum. The most dramatic morphological changes after injury were observed in the deeper aspects of the corpus callosum (mid-lower area of the corpus callosum in **Figure 2B**) compared with the sham-operated rat (**Figure 2A**). We observed a decrease in number of myelinated axons, and an increase in extra-axonal space, most likely due to axonal degeneration and glial cell activation (**Figure 2B**). In contrast, the superficial aspects of the corpus callosum (mid-upper area of the corpus callosum close to the cingulum in **Figure 2B**) had highly organised axonal bundles travelling intertwined in the left-right direction in the cutting plane with a slight decrease in the number of myelinated axons (**Figure 2B**). These observations were consistent in both TBI rats with slightly more extensive changes observed in TBI #2.

The DEC-FA maps revealed a decrease in FA in the corpus callosum after TBI (**Figure 4D**) compared with the sham-operated rat (**Figure 4A**). The orientation of the water diffusion in the location of the SBEM sample was a mixture of medio-lateral and dorso-caudal orientations in the sham-operated animal (**Figure 4A**), but in TBI animals, the orientation contained a slightly different contribution of medio-lateral and dorso-caudal orientations (**Figure 4D**). Diffusion ellipsoids, anisotropy values, and angular differences between the DTI and SBEM orientation vectors from the ipsi- and contralateral corpus callosum in sham-operated and TBI rats are shown

in **Figure 5**. FA values in the TBI animals were generally lower both ipsilaterally (TBI #1 = 0.72; TBI #2 = 0.64) and contralaterally (TBI #1 = 0.71; TBI #2 = 0.69) than the corresponding values in the sham-operated rat (Ipsi = 0.86; Contra = 0.84; **Figure 5B**). The ipsi- and contralateral values were similar in TBI #1, whereas the ipsilateral FA values were slightly lower than the contralateral FA values in TBI #2. Also, the decrease in anisotropy was more extensive in TBI #2 compared with TBI #1. The 3D-FT analysis of the corpus callosum performed by selecting the whole volume of the corpus callosum in the dataset (**Figure 2A**) showed that the AI values of the ipsi- and contralateral corpus callosum of the TBI animals were slightly lower (TBI #1: 0.46 and 0.47; TBI #2: 0.47 and 0.48) than those from the sham-operated animal (Ipsi = 0.48; Contra = 0.50; **Figure 5B**). In contrast to the cingulum, the differences in FA values between sham-operated and TBI animals were not reflected in the corpus callosum, to a great extent, by the 3D-FT analysis of SBEM datasets.

The angular difference between the orientation of the principal eigenvectors from DTI and SBEM in the corpus callosum varied between 2.0° and 21.9° (**Figure 5B**). The main orientation was consistent in both methods, as shown by the diffusion ellipsoids (**Figure 5B**). The main orientation in DTI and SBEM in sham-operated and TBI rats was a mixture of medio-lateral and dorso-caudal orientations. The major orientation of the two TBI animals, however, was different. TBI #1 showed a greater contribution of the medio-lateral orientation, while TBI #2 showed a greater dorso-ventral orientation contribution, as compared with the sham-operated rat (**Figure 5B**). These differences were more evident ipsilaterally than contralaterally.

Qualitative and quantitative analyses of grey matter: perilesional cortex

Six months after TBI, the perilesional cortex showed marked cellular alterations (**Figure 3B**). We observed neuronal swelling with shortened and deformed dendrites, and activated glial cells with

a high number of vacuoles. In the TBI rats, the number of myelinated axons had dramatically decreased in the cortex as well as in the external capsule (**Figure 3B**).

The ipsilateral deep layers of the cortex of TBI rats showed a decrease in FA values compared with the ipsilateral cortex in the sham-operated rat (**Figure 6A, 6D**). The orientation of the water diffusion in voxels from the layer VI dramatically changed, mainly from the rostro-caudal orientation in the sham-operated rat to include contributions of the other orientations (**Figure 6D**).

Diffusion ellipsoids, anisotropy values, and angular differences between DTI and SBEM orientation vectors from the ipsi- and contralateral perilesional cortical layer VI in the sham-operated rat and TBI rats are shown in **Figure 7**. The FA value from the ipsilateral cortex of TBI #1 was considerably higher (Ipsi = 0.41) than the corresponding values on the contralateral side (Contra = 0.26) and the sham-operated animal (Ipsi = 0.18; Contra = 0.30; **Figure 7**). The FA value from the ipsilateral cortex of TBI #2 was slightly lower (Ipsi = 0.16) than the corresponding values at the contralateral site (Contra = 0.17) and in the sham-operated rat (**Figure 7**). These differences between the FA values in the two TBI rats might indicate a different stage in the degenerative processes in these two animals at this time-point.

The AI values obtained from 3D-FT analysis followed the same pattern of changes as described for the FA values (**Figure 7**). The AI value from the ipsilateral cortex of TBI #1 was higher (Ipsi = 0.20) than the corresponding values in the contralateral side (Contra = 0.24) and the sham-operated animal (Ipsi = 0.17; **Figure 7**). The AI value from the ipsilateral cortex of TBI #2 was lower (Ipsi = 0.12) than the corresponding values in the contralateral side (Contra = 0.20) and the sham-operated rat (**Figure 7**).

The angular difference between the orientation of the principal eigenvectors from DTI and SBEM in the perilesional layer VI varied between 3.8° and 15.7° (**Figure 7**). The orientation provided by SBEM analysis from the cortical samples matched the orientation provided by DTI (**Figure 7**). In the sham-operated rat, we observed differences in the orientation between the ipsi- and the contralateral sides. The differences between ipsi- and contralateral orientations in the cortical layer VI might indicate a permanent effect of the sham operation on the cortex. In TBI rats, differences between ipsi- and contralateral sides were evident, and more importantly, differed between the two injured animals. In TBI #1, the orientation of the ipsilateral layer VI was a mixture of medio-lateral and rostro-caudal orientations, while on the contralateral side the contribution of the dorso-ventral orientation had increased (**Figure 7**). In TBI #2, the orientation of the ipsilateral Layer VI was dorso-ventral with a small contribution of medio-lateral orientation, while the contralateral side had the opposite, a medio-lateral orientation with a small contribution of the dorso-ventral orientation (**Figure 7**).

Comparison between low and high magnification SBEM data acquisitions

To test the stability of the 3D-FT analysis, an additional dataset was acquired from the corpus callosum (**Figure 4C and 4F**) and the cortex (**Figure 6C and 6F**) simultaneously with higher in-plane resolution. The AI values and angular differences from the low and high magnification SBEM datasets from the corpus callosum and perilesional cortex are summarised in **Table 1**. In the corpus callosum, the AI values were consistent in both low and high magnification datasets from the contralateral (LM = 0.51, HM = 0.52) and ipsilateral (LM = 0.47, HM = 0.48) side in the sham-operated rat, and from the contralateral (LM = 0.50, HM = 0.51) and ipsilateral (LM = 0.55, HM = 0.55) side of the TBI rat (**Table 1**). While the angular difference between DTI and SBEM principal eigenvector was between 0° to 1.1°, the angular difference in V2 and V3 varied between 0.6° to

28.1° (**Table 1**). In the perilesional cortex, AI values were also consistent in the low and high magnification datasets in the contralateral side in both sham-operated (LM = 0.33, HM = 0.33) and TBI (LM = 0.28, HM = 0.28) animals (**Table 1**). In the ipsilateral side, high magnification AI values were higher than the corresponding low magnification AI values in both sham-operated (LM = 0.17, HM = 0.20) and TBI (LM = 0.10, HM = 0.15) rats (**Table 1**). The angular difference between the principal eigenvector obtained with these two modalities remained small from 4.6° to 9.7° (**Table 1**). The angular difference in V2 and V3 was higher than for V1 with values between 1.1° to 37.2° (**Table 1**).

Discussion

The present work is the first proof-of-concept study using mesoscale SBEM data to validate DTI metrics. We implemented 3D-FT analysis on SBEM datasets, which extracts the anisotropy and orientation data of tissue that correlate with the FA and orientation data generated by DTI. We established a workflow that included DTI and SBEM imaging from the same brains by co-localizing the SBEM tissue samples to the DTI images, which allowed us to pinpoint the voxels in the DTI maps. The main achievement in our study is that this is the first proof-of-concept demonstration that 3D EM data could be obtained from a volume with a size on the order of an imaging voxel. We obtained tissue metrics, i.e., anisotropy and orientation, using DTI and 3D-FT methods from sham-operated and TBI rats from two white matter areas (cingulum and corpus callosum) and one grey matter area (layer VI of the perilesional cortex). The parameters derived from the SBEM data were mostly in good agreement with the corresponding DTI indices. These results demonstrated that the SBEM method in combination with 3D-FT analysis can produce quantitative metrics, and paves the way to a more sophisticated validation of more advanced diffusion MRI contrasts.

SBEM as a method to investigate the tissue microstructure at the level of the DTI voxel

SBEM is a powerful technique for studying the ultrastructure and local neural circuits of brain tissue (**Denk and Horstmann 2004; Denk et al. 2012; Helmstaedter 2013**). The en-block staining, backscattering contrast, and high-resolution of SBEM provide great contrast for visualizing cellular membranes. In addition, the large field of view and resolution provided by SBEM fills the gap between the traditional small sample size of electron microscopy and the large areas of light microscopy. Although SBEM provides larger volumes than other 3D block-face electron microscopy techniques, such as focused-ion beam milling imaging, it is still limited to volumes up to 1 mm^3. This size limitation challenges the co-registration of the SBEM datasets to the DTI images. To accurately co-localise the tissue block in DTI maps, we performed a co-registration of the SBEM datasets using photomicrographs of all the steps of the sample preparation and during the imaging. There were steps in the sample preparation, such as trimming or mounting of the block, tissue shrinkage after staining, or partial-volume effect in DTI voxels, however, which are potential sources of error (ranging from small to moderate) of angular differences between the DTI and SBEM vectors. Therefore, the co-registration might have inaccuracies and a more systematic, statistics-based, approach with a greater number of samples should be implemented in future studies. SBEM provides a new opportunity to investigate the contribution of the specific cellular components responsible for the DTI contrast, thus making it an excellent tool in validating advanced diffusion MRI methods estimating properties of microstructure, such as CHARMED (**Assaf et al., 2004**), NODDI (**Zhang et al., 2012**), RSI (**White et al., 2013**), qMAS (**Lasič et al., 2014; Szczepankiewicz et al., 2015**), and DIAMOND (**Scherrer et al., 2016**). This method requires automatic and specific segmentation methods that are not yet available for such large datasets. In the future, annotation of individual cellular components will allow us to resolve and quantify in more detail the microstructure underlying the DTI contrast.

Validation of the DTI metrics using 3D-FT analysis

Fourier transform-based analysis was recently introduced in 2D histological sections. 2D-FT analysis extracted tissue metrics of histologically stained sections of normal and pathological brain after brain injury or status epilepticus (**Budde et al., 2011; Salo et al., 2017**). In particular, our previous study demonstrated that 2D-FT anisotropy and orientation data from histological preparations can be directly correlated to DTI metrics during epileptogenesis (**Salo et al., 2017**). Here, we expand our previous 2D study by extracting anisotropy and orientation data of cellular components using 3D-FT analysis in SBEM datasets.

In the present study, we obtained 3D tissue metrics from the cingulum, corpus callosum, and perilesional cortical layer VI of sham-operated and TBI brains in a chronic phase after the injury. In our previous studies, we demonstrated that microstructural alterations are persistent in grey and white matter at this chronic time-point (**Laitinen et al. 2015; Lehto et al. 2017**). Many previous studies used transmission electron microscopy to characterise TBI pathology of tissue (**Dietrich et al. 1994; Rodriguez-Paez et al. 2005; Mac Donald et al. 2007; Reeves et al. 2012**). The present study, however, is the first to use a 3D technique to explore the microstructural alterations in cellular components after TBI on a scale that is comparable to the MRI voxel.

Despite the small angular differences between the DTI and FT methods in both white and grey matter areas, the orientation obtained from the 3D-FT analysis was in good agreement with the orientation obtained from DTI. The anisotropy values obtained from the perilesional cortex were consistent in both methods, however, in the white matter areas, the AI values were consistently lower than the corresponding FA values. The main reason for this discrepancy might be the intrinsic difference between the DTI and FT methods. Whereas DTI reveals anisotropy of the diffusion of water molecules, the FT analysis provides a measure of anisotropy of the staining intensity changes in the SBEM images. Khan et al. (**2015**) noted a potentially related discrepancy,

in which structure tensor anisotropy did not associate with diffusion MRI anisotropy in the inferior longitudinal fasciculus. Sample preparation for SBEM, including staining with heavy metals, dehydration, and embedding of the tissue samples, might also affect the anisotropy value. The sample preparation might influence the anisotropy more in the white matter than in the grey matter due to differences in the cellular environments. In white matter, the highly organized and densely packed axons and the high lipid content of the myelin dominate, while in the grey matter, cell bodies and neuropil are the main components. Regardless of these differences in anisotropy, the intrinsic variation in the anisotropy due to TBI followed the same pattern for both DTI and SBEM in all areas evaluated.

We used the classical and most commonly used diffusion tensor model, which is based in the b-value formalism and assumes a Gaussian distribution of water displacement due to diffusion, which is equivalent to the 3D-FT analysis presented here. In both methods, the intravoxel information is averaged, which makes them inadequate for characterizing diffusion in voxels with a complex fibre structure (**Wiegell et al., 2000**). Therefore, some studies have introduced more complex models in 2D stained sections by manually tracing fibres (**Leergaard et al., 2010; White et al., 2013**), using structure tensor analysis (**Budde and Frank, 2012; Budde and Annese, 2013**), or Fourier domain filter matching (**Choe et al., 2012**). The tissue is inherently three-dimensional, however, restricting the use of 2D analyses in areas where tissue orientation coincides with section orientation. Recent studies utilised 3D light microscopy to validate diffusion MRI contrast (**Wang et al., 2014; Khan et al., 2015; Wang et al., 2015; Schilling et al., 2016**). Khan and collaborators presented a 3D structure tensor method analysing DiI-stained sections using confocal microscopy (**Khan et al., 2015**). Schilling and collaborators presented the fibre orientation distribution from DiI-stained sections using confocal microscopy (**Schilling et al., 2016**). Light microscopy techniques are excellent tools for studying macrostructural tissue properties in a large

range of areas, from the microstructural level (a few μm^2) to whole brain sections. Future studies will focus on implementing more complex methods for analysing SBEM datasets to study the complexity of intravoxel information, such as structure tensors (**Budde and Frank, 2012**), and comparing results with, e.g., q-ball (**Tuch, 2004**) and/or constrained spherical deconvolution (**Tournier et al., 2007**) methods.

Low magnification versus high magnification of SBEM datasets

To evaluate the robustness of our 3D-FT approach we tested it in SBEM datasets acquired at low and high magnification. The AI values obtained from the corpus callosum and perilesional cortex matched when measured with low and high magnification. Also, in the corpus callosum, there was practically no angular difference of the principal axis between the two resolutions. In the more complex environment of the cortex, we obtained larger differences in orientations, most likely due to more detailed image information provided by the higher resolution dataset. Our findings revealed that the resolution of low magnification datasets was sufficient to capture the main features in our 3D-FT analysis. For the implementation of new analytical methods for SBEM datasets in very heterogeneous environments such as the cortex, however, a higher resolution may be needed to encapsulate the full extent of the diffusion barriers.

Conclusion

Here we demonstrate the ability to perform 3D-FT analyses on SBEM data of the white and grey matter in sham-operated and TBI rats. The advantage of SBEM data relative to conventional histological preparations derives from the ability to visualise all the barriers to the diffusion of water molecules (membranes of cellular components) in 3D and high-resolution. The tissue metrics, AI and orientation, extracted from the 3D-FT in SBEM reflected changes in the DTI

metrics, FA and orientation. This study provides new methods for investigating the DTI contrast from a microstructural perspective and can be extended to more advanced diffusion MRI approaches with more sophisticated analyses in the future.

Acknowledgments

This work was supported by the Academy of Finland (#275453 AS, #298007 OG), and Biocenter Finland and University of Helsinki (IB, EJ, and SBEM imaging). We would like to thank Maarit Pulkkinen for her help with the animal handling, Mervi Lindman and Antti Salminen for help preparing the samples for SBEM, and Dr. Jaakko Paasonen for video editing.

Author contributions

A.S., O.G., and E.J. contributed to the concept and study design; I.B. and E.M. collected the SBEM and DTI data, respectively; R.A.S. and A.S. performed the analyses; R.A.S., O.G., and A.S. interpreted the data; R.A.S., A.S., and O.G. wrote the main manuscript text; all authors reviewed the manuscript.

Competing financial interests

The authors declare that they have no competing interests.

References

Aggarwal, M., Nauen, D.W., Troncoso, J.C., Mori, S., 2015. Probing region-specific microstructure of human cortical areas using high angular and spatial resolution diffusion MRI. Neuroimage, 105, 198-207.

Assaf, Y., Freidlin, R.Z., Rohde, G.K., Basser, P.J., 2004. New modeling and experimental framework to characterize hindered and restricted water diffusion in brain white matter. Magn. Reson. Med. 52(5), 965-978.

Axer, M., Amunts, K., Grässel, D., Palm, C., Dammers, J., Axer, H., Pietrzyk, U., Zilles, K., 2011. A novel approach to the human connectome: ultra-high resolution mapping of fiber tracts in the brain. Neuroimage, 54(2), 1091-1101.

Axer, M., Strohmer, S., Gräßel, D., Bücker, O., Dohmen, M., Reckfort, J., Zilles, K., Amunts, K., 2016. Estimating fiber orientation distribution functions in 3D-polarized light imaging. Front. Neuroanat. 10.

Basser, P.J., Mattiello, J., LeBihan, D., 1994. MR diffusion tensor spectroscopy and imaging. Biophys. J. 66(1), 259-267.

Basser, P. J., Pierpaoli, C., 1996. Microstructural and physiological features of tissues elucidated by quantitative-diffusion-tensor MRI. J. Magn. Reson. B, 111(3), 209-219.

Belevich, I., Joensuu, M., Kumar, D., Vihinen, H., Jokitalo, E., 2016. Microscopy image browser: a platform for segmentation and analysis of multidimensional datasets. PLoS Biol. 14(1), e1002340.

Budde, M.D., Janes, L., Gold, E., Turtzo, L.C., Frank, J.A., 2011. The contribution of gliosis to diffusion tensor anisotropy and tractography following traumatic brain injury: validation in the rat using Fourier analysis of stained tissue sections. Brain, 134(8), 2248-2260.

Budde, M.D., Frank, J.A., 2012. Examining brain microstructure using structure tensor analysis of histological sections. Neuroimage, 63(1), 1-10.

Budde, M.D., Annese, J., 2013. Quantification of anisotropy and fiber orientation in human brain histological sections. Front. Integr. Neurosci. 7, 3.

Chazotte, B., 2011. Labeling membranes with carbocyanine dyes (DiIs) as phospholipid analogs. Cold Spring Harbor Protocols, 2011(1), pdb-prot5555.

Chang, E.H., Argyelan, M., Aggarwal, M., Chandon, T.S.S., Karlsgodt, K.H., Mori, S., Malhotra, A.K., 2017. Diffusion tensor imaging measures of white matter compared to myelin basic protein immunofluorescence in tissue cleared intact brains. Data in brief, 10, 438-443.

Chang, E.H., Argyelan, M., Aggarwal, M., Chandon, T.S.S., Karlsgodt, K.H., Mori, S., Malhotra, A.K., 2017. The role of myelination in measures of white matter integrity: combination of diffusion tensor imaging and two-photon microscopy of CLARITY intact brains. NeuroImage, 147, 253-261.

Choe, A.S., Stepniewska, I., Colvin, D.C., Ding, Z., Anderson, A.W., 2012. Validation of diffusion tensor MRI in the central nervous system using light microscopy: quantitative comparison of fiber properties. NMR Biomed. 25(7), 900-908.

Dauguet, J., Delzescaux, T., Condé, F., Mangin, J.F., Ayache, N., Hantraye, P., Frouin, V., 2007. Three-dimensional reconstruction of stained histological slices and 3D non-linear registration with in-vivo MRI for whole baboon brain. J. Neurosci. Methods, 164(1), 191-204.

Deerinck, T.J., Bushong, E.A., Lev-Ram, V., Shu, X., Tsien, R.Y., Ellisman, M.H., 2010. Enhancing serial block-face scanning electron microscopy to enable high resolution 3-D nanohistology of cells and tissues. Microsc. Microanal. 16(S2), 1138-1139.

Denk, W., Briggman, K.L., Helmstaedter, M., 2012. Structural neurobiology: missing link to a mechanistic understanding of neural computation. Nat. Rev. Neurosci. 13(5), 351-358.

Denk, W., Horstmann, H., 2004. Serial block-face scanning electron microscopy to reconstruct three-dimensional tissue nanostructure. PLoS Biol. 2(11), e329.

Dietrich, W.D., Alonso, O., Halley, M., 1994. Early microvascular and neuronal consequences of traumatic brain injury: a light and electron microscopic study in rats. J. neurotrauma, 11(3), 289-301.

Helmstaedter, M., 2013. Cellular-resolution connectomics: challenges of dense neural circuit reconstruction. Nature methods, 10(6), 501-507.

Helmstaedter, M., Briggman, K.L., Denk, W., 2008. 3D structural imaging of the brain with photons and electrons. Curr. opin. Neurobiol. 18(6), 633-641.

Jespersen, S.N., Leigland, L.A., Cornea, A., Kroenke, C.D., 2012. Determination of axonal and dendritic orientation distributions within the developing cerebral cortex by diffusion tensor imaging. IEEE Trans. Med. Imaging, 31(1), 16-32.

Josso, B., Burton, D.R., Lalor, M.J., 2015. Texture orientation and anisotropy calculation by Fourier transform and principal component analysis. Mech Syst Signal Process, 19(5), 1152-1161 (2005).

Khan, A.R., Cornea, A., Leigland, L.A., Kohama, S.G., Jespersen, S.N., Kroenke, C.D., 2015. 3D structure tensor analysis of light microscopy data for validating diffusion MRI. Neuroimage, 111, 192-203.

Kharatishvili, I., Nissinen, J.P., McIntosh, T.K., Pitkänen, A., 2006. A model of posttraumatic epilepsy induced by lateral fluid-percussion brain injury in rats. Neuroscience, 140(2), 685-697.

Lasič, S., Szczepankiewicz, F., Eriksson, S., Nilsson, M., Topgaard, D., 2014. Microanisotropy imaging: quantification of microscopic diffusion anisotropy and orientational order parameter by diffusion MRI with magic-angle spinning of the q-vector. Frontiers in Physics, 2, 11.

Le Bihan, D., 2003. Looking into the functional architecture of the brain with diffusion MRI. Nat Rev. Neurosci. 4(6), 469-480.

Laitinen, T., Sierra, A., Pitkänen, A., Gröhn, O., 2010. Diffusion tensor MRI of axonal plasticity in the rat hippocampus. Neuroimage, 51(2), 521-530.

Laitinen, T., Sierra, A., Bolkvadze, T., Pitkänen, A., Gröhn, O., 2015. Diffusion tensor imaging detects chronic microstructural changes in white and gray matter after traumatic brain injury in rat. Front. neurosci. 9, 128.

Leergaard, T.B., White, N.S., De Crespigny, A., Bolstad, I., D'Arceuil, H., Bjaalie, J.G., Dale, A.M., 2010. Quantitative histological validation of diffusion MRI fiber orientation distributions in the rat brain. PloS one, 5(1), e8595.

Lehto, L.J., Sierra, A., Gröhn, O, 2017. Magnetization transfer SWIFT MRI consistently detects histologically verified myelin loss in the thalamocortical pathway after a traumatic brain injury in rat. NMR Biomed. 30(2).

Mac Donald, C.L., Dikranian, K., Bayly, P., Holtzman, D., Brody, D., 2007. Diffusion tensor imaging reliably detects experimental traumatic axonal injury and indicates approximate time of injury. J. Neurosci. 27(44), 11869-11876.

Marquez, J.P., 2006. Fourier analysis and automated measurement of cell and fiber angular orientation distributions. Int. J. Solids. Struct. 43(21), 6413-6423.

Rodriguez-Paez, A.C., Brunschwig, J.P., Bramlett, H.M., 2005. Light and electron microscopic assessment of progressive atrophy following moderate traumatic brain injury in the rat. Acta neuropathol. 109(6), 603-616.

Reeves, T.M., Smith, T.L., Williamson, J.C., Phillips, L.L., 2012. Unmyelinated axons show selective rostrocaudal pathology in the corpus callosum after traumatic brain injury. J. Neuropathol. Exp. Neurol. 71(3), 198-210.

Salo, R.A., Miettinen, T., Laitinen, T., Gröhn, O., Sierra, A., 2017. Diffusion tensor MRI shows progressive changes in the hippocampus and dentate gyrus after status epilepticus in rat – histological validation with Fourier-based analysis. NeuroImage 152, 221-236.

Scherrer, B., Schwartzman, A., Taquet, M., Sahin, M., Prabhu, S.P., Warfield, S.K., 2016. Characterizing brain tissue by assessment of the distribution of anisotropic microstructural environments in diffusion-compartment imaging (DIAMOND). Magn. Reson. Med. 76(3), 963-977.

Schilling, K., Janve, V., Gao, Y., Stepniewska, I., Landman, B.A., Anderson, A.W., 2016. Comparison of 3D orientation distribution functions measured with confocal microscopy and diffusion MRI. Neuroimage, 129, 185-197.

Sierra, A., Laitinen, T., Gröhn, O., Pitkänen, A., 2015. Diffusion tensor imaging of hippocampal network plasticity. Brain Struct. Func. 220(2), 781-801.

Szczepankiewicz, F., Lasič, S., van Westen, D., Sundgren, P.C., Englund, E., Westin, C.F., Ståhlberg, F., Lätt, J., Topgaard, D., Nilsson, M., 2015. Quantification of microscopic diffusion anisotropy disentangles effects of orientation dispersion from microstructure: applications in healthy volunteers and in brain tumors. NeuroImage, 104, 241-252.

Tournier, J.D., Calamante, F., Connelly, A., 2007. Robust determination of the fibre orientation distribution in diffusion MRI: non-negativity constrained super-resolved spherical deconvolution. Neuroimage, 35(4), 1459-1472.

Tuch, D.S., 2004. Q-ball imaging. Magnetic resonance in medicine, 52(6),1358-1372.

Wang, H., Zhu, J., Reuter, M., Vinke, L.N., Yendiki, A., Boas, D.A., Fischl, B., Akkin, T., 2014. Cross-validation of serial optical coherence scanning and diffusion tensor imaging: a study on neural fiber maps in human medulla oblongata. Neuroimage, 100, 395-404.

Wang, H., Lenglet, C., Akkin, T., 2015. Structure tensor analysis of serial optical coherence scanner images for mapping fiber orientations and tractography in the brain. J. Biomed. Opt. 20(3), 036003-036003.

White, N.S., Leergaard, T.B., D'Arceuil, H., Bjaalie, J.G., Dale, A.M., 2013. Probing tissue microstructure with restriction spectrum imaging: histological and theoretical validation. Hum. Brain. Mapp. 34(2), 327-346.

Wiegell, M.R., Larsson, H.B., & Wedeen, V.J., 2000. Fiber crossing in human brain depicted with diffusion tensor MR imaging 1. Radiology, 217(3), 897-903.

Zhang, H., Schneider, T., Wheeler-Kingshott, C.A., Alexander, D.C., 2012. NODDI: practical in vivo neurite orientation dispersion and density imaging of the human brain. Neuroimage, 61(4), 1000-1016.

Figure legends

Figure 1: Co-registration of the directionally-encoded colour (DEC)-fractional anisotropy (FA) maps and 1-mm thick histological sections (A-C), and pipeline for sample preparation for SBEM imaging (D-G). (**A**) A representative example of a DEC-FA map of an animal 5 months after TBI. (**B**) 1-mm thick section of the same animal after whole brain sectioning. (**C**) Co-registration of the FA map and 1-mm thick section shown in panels **A** and **B**. Directions for directionally-encoded colours are *green* rostral-caudal, *red* lateral-medial, and *blue* dorsal-ventral in panel **A**. (**D**) A representative 500-nm semi-thin section from a sample including the cingulum and corpus callosum block co-registered to the 1-mm thick section. The red rectangle indicates the area shown in panel **E**. (**E**) Morphological landmarks (vessels) on the 500-nm semi-thin sections in the cingulum and corpus callosum. (**F**) Morphological landmarks on the block-face in an SBEM overview image revealing the same features as in panel **E**. The red rectangles indicate the location of the low and high magnification data sets shown in panel **G**. (**G**) Low (grey) and high (red-yellow) magnification SBEM datasets from the block shown in panels **D**-**F**. Scale bars: 1500 µm in panels **A**-**C**, 500 µm in panel **D**, 50 µm in panels **E**-**F**, and 25 µm in panel **G**.

Figure 2: Representative images from SBEM datasets of the ipsilateral cingulum and corpus callosum of a sham-operated rat (A) and TBI #2 (B). Red rectangles indicate the volumes-of-interest (VOI) for the cingulum and corpus callosum. Arrows point to in-plane individual axons, arrowheads to extra-axonal space, and asterisks indicate cell bodies. Note that both the corpus callosum and cingulum are formed by the high density of myelinated axons. These two areas have intrinsically different morphologies, highly parallel axons perpendicular to the x-y plane in the

cingulum, and crossing bundles of axons running closely to the x-y plane in the corpus callosum, which allowed us to test the potential of 3D-FT analysis. Scale bar: 10 µm. Abbreviation: V, vessel.

Figure 3: Representative images from SBEM datasets of the ipsilateral layer VI of the perilesional cortex of the sham-operated rat (A) and TBI #2 (B). Red rectangles indicate the volumes-of-interest (VOI) for the cingulum and the corpus callosum. Arrows point to in-plane individual axons, arrowheads to extra-axonal space, and asterisks indicate cell bodies. Scale bar: 10 µm. Abbreviation: V, vessel.

Figure 4: Representative examples of images from DTI and SBEM data of the ipsilateral corpus callosum of the sham-operated rat and TBI #2. DEC-FA maps of the ipsilateral corpus callosum of the sham-operated rat (**A**) and TBI #2 (**D**). White squares indicate the voxels selected for analysis, confirmed by co-registration in the corpus callosum and cingulum. Directions for directionally-encoded colours are *green* rostral-caudal, *red* lateral-medial, and *blue* dorsal-ventral, and the colour intensity reflects the FA values. Close-up view of the low magnification SBEM dataset from the same sham-operated (**B**) and TBI (**E**) animals shown in panels **A** and **D**, respectively. Note that these views are only a part of the full dataset. White arrows indicate myelinated axons running in-plane, and white arrowheads, axons running in a rostro-caudal direction. The orange square highlights the location of the high magnification dataset. Scale bar: 20 µm. High magnification SBEM from the same sham-operated (**C**) and TBI (**F**) animals shown in panels **B** and **E**, respectively. Asterisks indicate individual axons, and white arrowheads point to the increase in the extra-axonal space in the animal after TBI. Scale bar: 3 µm. Abbreviations: cc, corpus callosum; cg, cingulum; Cx, cortex; HC, hippocampus; m, mitochondria; my, myelin; Olig, oligodendrocyte; V, vessel.

Figure 5: Diffusion ellipsoids, anisotropy values from DTI and 3D-FT analysis, and angular difference between the principal eigenvector in DTI and 3D-FT analysis in the cingulum (A) and corpus callosum (B). Directions for directionally encoded colours are *green* rostral-caudal, *red* lateral-medial, and *blue* dorsal-ventral. *Smaller SBEM dataset.

Figure 6: Representative examples of DTI and SBEM data from the ipsilateral perilesional cortex (layer VI) of the sham-operated rat and TBI #2. DEC-FA maps of the ipsilateral perilesional cortex in the sham-operated rat (**A**) and TBI #2 (**D**). White squares indicate the voxels selected for analysis confirmed by co-registration. Directions for directionally-encoded colours are *green* rostral-caudal, *red* lateral-medial, and *blue* dorsal-ventral, and the colour intensity reflects the FA values. Close-up view of the low magnification SBEM dataset from the same sham (**B**) and TBI (**E**) animals shown in the DEC-FA maps in panels **A** and **D**. The orange square highlights the location of the high magnification dataset. White arrows indicate myelinated axons, white arrowheads indicate dendrites and asterisks indicate neuronal cell bodies. Scale bar: 20 µm. High magnification SBEM from the same sham (**C**) and TBI (**F**) animals shown in the DEC-FA maps in panels **B** and **E**. Scale bar: 3 µm.

Figure 7: Diffusion ellipsoids, anisotropy values from DTI and 3D-FT analysis, and angular difference between principal eigenvector in DTI and 3D-FT analysis in the perilesional cortex (layer VI). Directions for directionally-encoded colours are *green* rostral-caudal, *red* lateral-medial, and *blue* dorsal-ventral. *Smaller SBEM datasets.

Table 1: Anisotropy and angular difference (degrees) of orientation vectors from 3D-FT analysis of SBEM low and high magnification datasets in the corpus callosum and perilesional cortex. Abbreviations: LM, low magnification; HM, high magnification.

Supplementary video 1: Visualisation of 3D SBEM images of contralateral cortex of sham-operated rat. Greyscale images show the stack of 3D SBEM images. Yellow-orange scale represents vessels, cell bodies, and dendrites. Green-blue scale shows myelin.

Supplementary video 2: Pipeline of the 3D-FT analysis. (**A**) A part of an SBEM dataset. (**B**) The same dataset Tukey-filtered with $\alpha = 0.2$. (**C**) The Tukey-filtered dataset after 3D Fourier transform. (**D**) An ellipsoid model of the Fourier-transformed dataset. Eigenvalues and -vectors from Eigen decomposition define the axes of the ellipsoid. (**E**) Ellipsoid from panel **D** with eigenvalues mirrored over the mean of the eigenvalues to correspond to the DTI model.

Corpus Callosum										
	Contralateral					Ipsilateral				
	Anisotropy		Angular difference			Anisotropy		Angular difference		
Animal	**LM**	**HM**	**V1**	**V2**	**V3**	**LM**	**HM**	**V1**	**V2**	**V3**
Sham	0.51	0.52	1.1	1.1	0.6	0.47	0.48	0.0	20.6	20.6
TBI #2	0.50	0.51	0.0	28.1	28.1	0.55	0.55	0.6	17.8	17.8
Perilesional cortex										
	Contralateral					Ipsilateral				
	Anisotropy		Angular difference			Anisotropy		Angular difference		
Animal	**LM**	**HM**	**V1**	**V2**	**V3**	**LM**	**HM**	**V1**	**V2**	**V3**
Sham	0.33	0.33	8.0	8.0	1.1	0.17	0.20	5.7	36.7	37.2
TBI #2	0.28	0.28	9.7	9.7	2.9	0.10	0.15	4.6	26.4	26.4

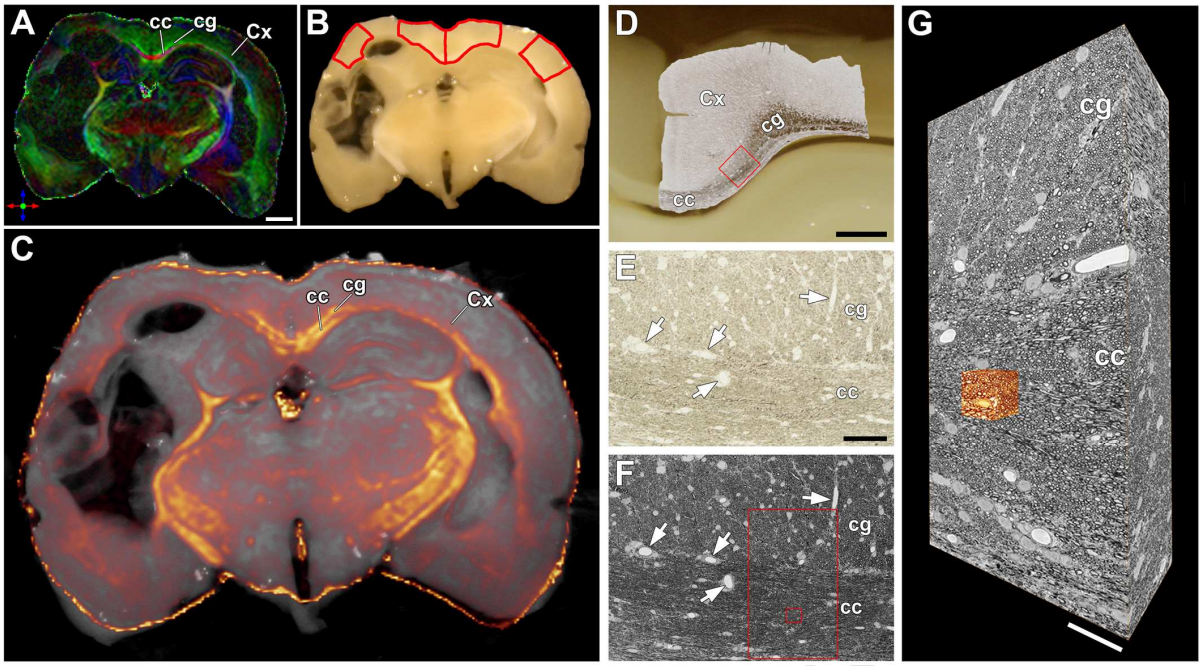

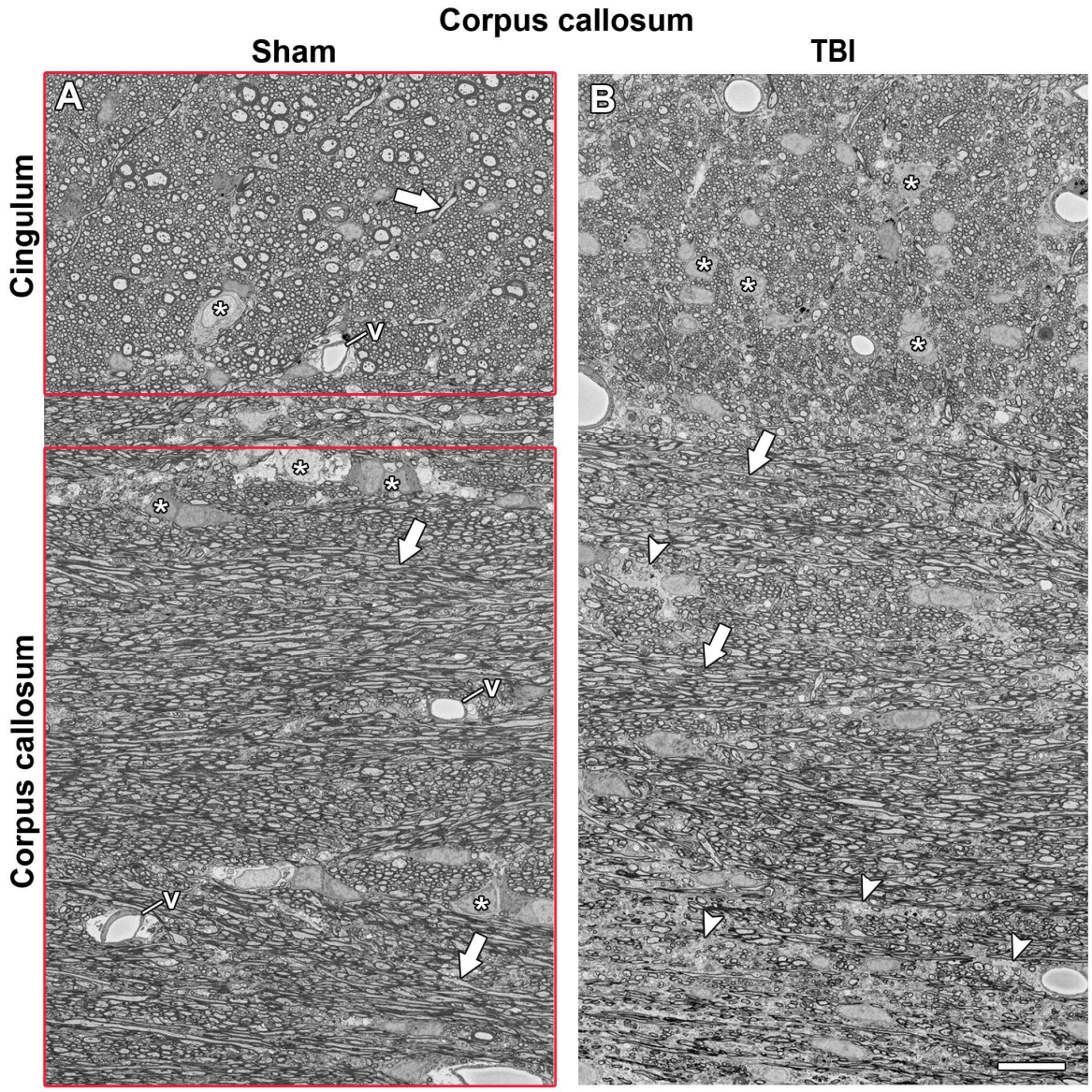

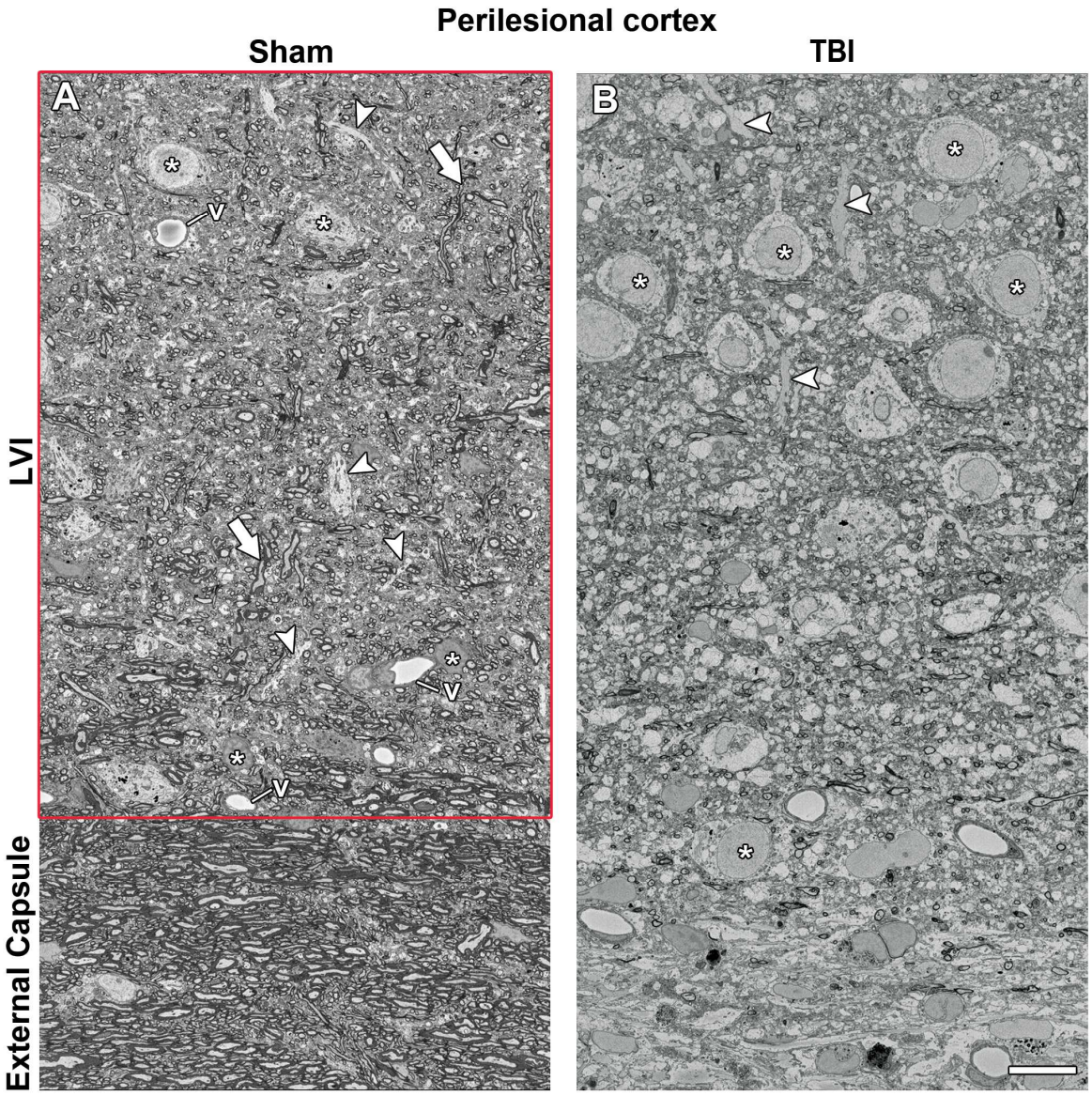

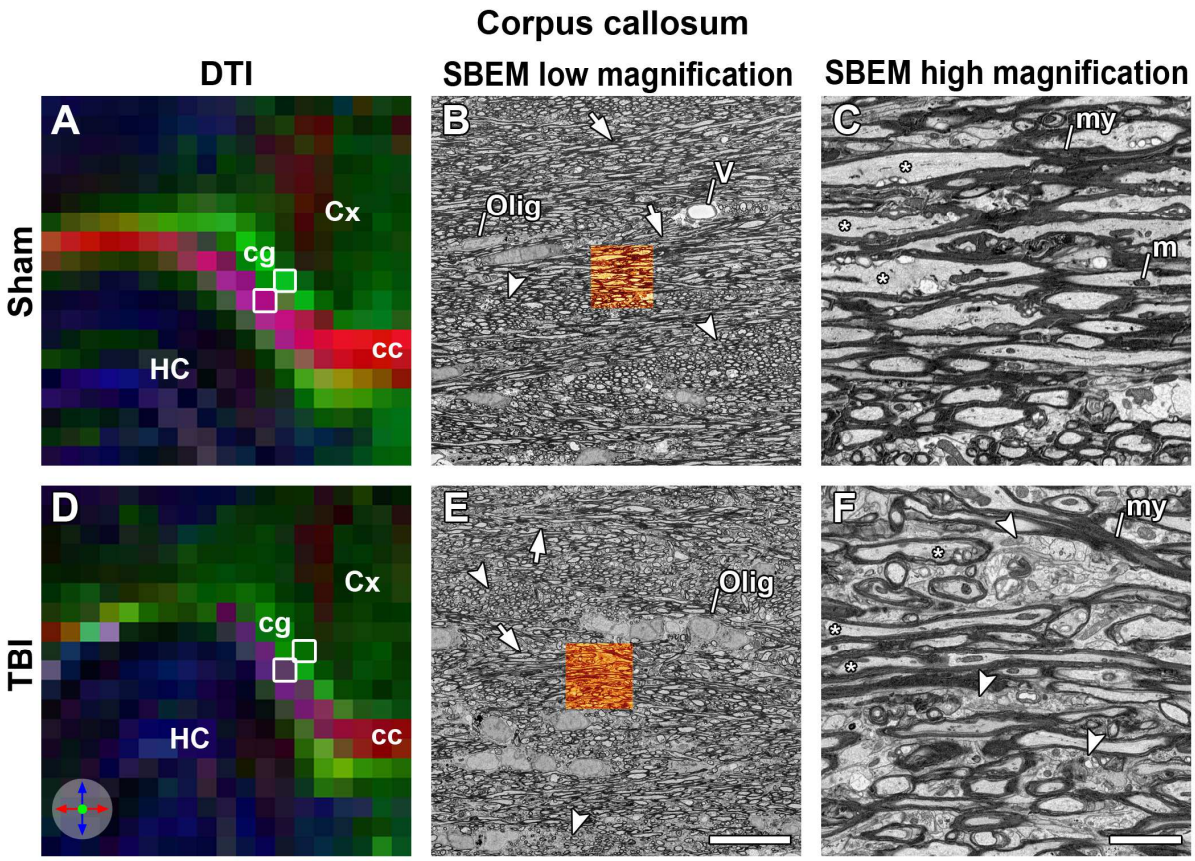

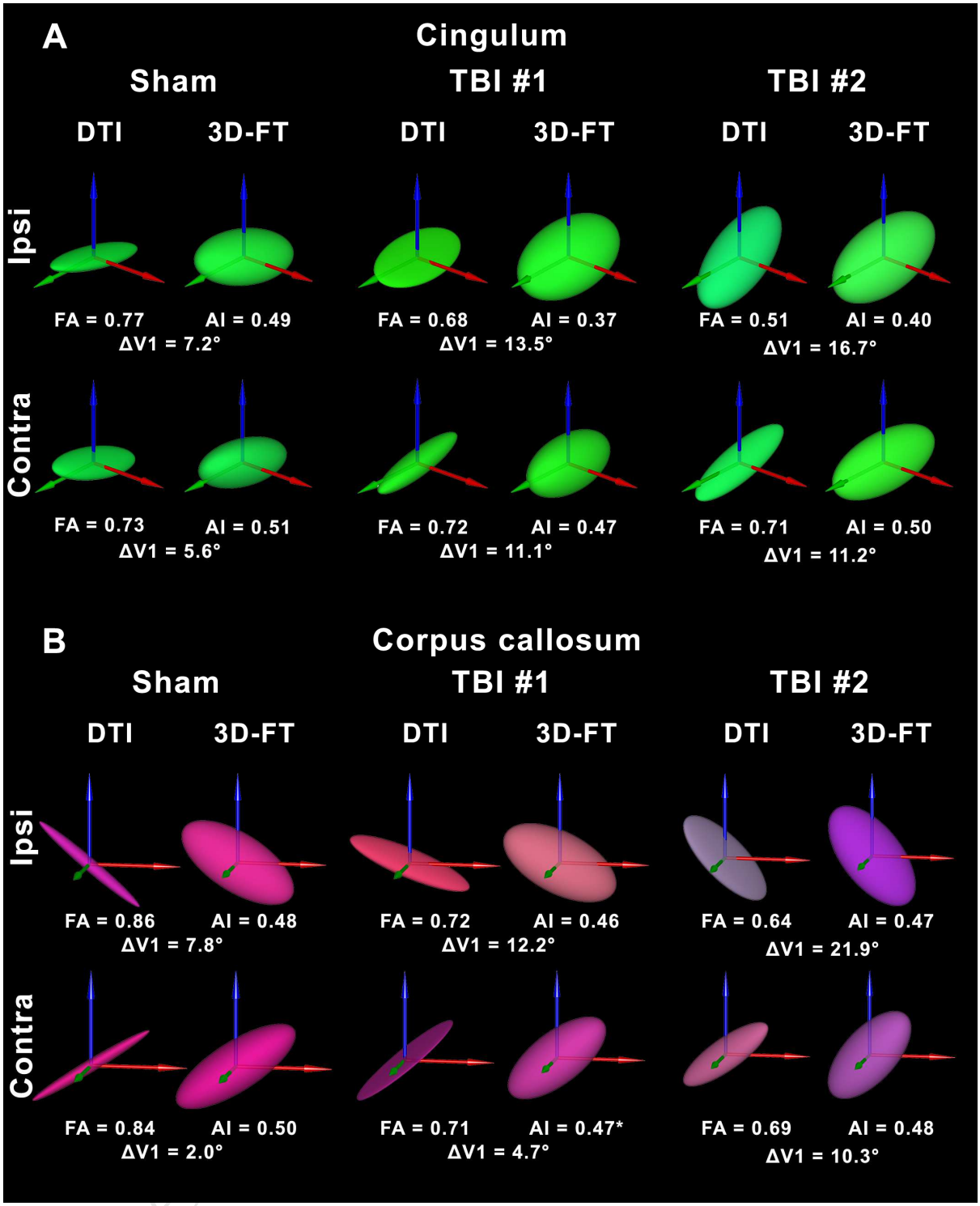
A
Cingulum
Sham
TBI #1
TBI #2
DTI
3D-FT
DTI
3D-FT
DTI
3D-FT
Ipsi
FA = 0.77
AI = 0.49
ΔV1 = 7.2°
FA = 0.68
AI = 0.37
ΔV1 = 13.5°
FA = 0.51
AI = 0.40
ΔV1 = 16.7°
Contra
FA = 0.73
AI = 0.51
ΔV1 = 5.6°
FA = 0.72
AI = 0.47
ΔV1 = 11.1°
FA = 0.71
AI = 0.50
ΔV1 = 11.2°
B
Corpus callosum
Sham
TBI #1
TBI #2
DTI
3D-FT
DTI
3D-FT
DTI
3D-FT
Ipsi
FA = 0.86
AI = 0.48
ΔV1 = 7.8°
FA = 0.72
AI = 0.46
ΔV1 = 12.2°
FA = 0.64
AI = 0.47
ΔV1 = 21.9°
Contra
FA = 0.84
AI = 0.50
ΔV1 = 2.0°
FA = 0.71
AI = 0.47*
ΔV1 = 4.7°
FA = 0.69
AI = 0.48
ΔV1 = 10.3°